PERGAMON

International Journal of Heat and Mass Transfer 44 (2001) 417–428

International Journal of HEAT and MASS TRANSFER

www.elsevier.com/locate/ijhmt

Heat transfer and fluid flow in a partially or fully penetrated weld pool in gas tungsten arc welding

H.G. Fan[a], H.L. Tsai[a,*], S.J. Na[b]

[a]*Department of Mechanical and Aerospace Engineering and Engineering Mechanics, University of Missouri-Rolla, Rolla, MO 65409, USA*

[b]*Department of Mechanical Engineering, Korea Advanced Institute of Science and Technology, Kusongdong 371-1, Yusonggu, Taejon 305-701, South Korea*

Received 24 September 1999; received in revised form 25 February 2000

Abstract

In this study, fluid flow driven by a combination of electromagnetic force, buoyancy force, arc drag force, and surface tension gradient is numerically analyzed for a partially or fully penetrated weld pool in stationary gas tungsten arc welding (GTAW). Irregular shape of the weld pool and the moving liquid–solid interface is handled by a boundary-fitted-coordinates technique. Surface tension on the top and the bottom free surfaces of the weld pool is found to play a critical role in determining the flow pattern in the weld pool. The calculated GTA weld bead geometry compares favorably with experimental results.

1. Introduction

In view of the significant effects of weld pool convection on the microstructure and properties of the resultant weld, numerous investigators have attempted to calculate heat transfer and fluid flow in the weld pool. Most of these investigators have used either the rigid-lid assumption [1–5] or the stepwise approximation [6–8] for the weld pool surface. In fact, the molten pool surface becomes depressed and its shape affects the weld formation at high welding currents. Tsai and Kou [9] used the finite difference method and pool surface fitting orthogonal curvilinear coordinates to calculate heat transfer and fluid flow in a weld pool, focusing on the effect of the electromagnetic force on pool surface deformation. Kim and Na [10], on the other hand, used the boundary fitted coordinates to calculate the pool surface shape, as well as heat transfer and fluid flow in the weld pool.

Convection in the weld pool is driven by a combination of forces, which includes the surface tension force, buoyancy force, electromagnetic force, and arc drag force. Most researchers have considered only three forces, excluding arc drag force, as the driving forces for the weld pool convection. It is indicated that arc drag force also plays an important role affecting convection in the weld pool [2]. In most cases, however, fluid flow and heat transfer in the weld pool are controlled by surface tension force. The presence of surface-active elements, such as sulfur or oxygen, in steels significantly alters the temperature coefficient of surface tension, $d\gamma/dT$, and thereby, the flow field in the weld pool [3].

Up to the present, far less work has been conducted on the heat transfer and fluid flow in gas

* Corresponding author. Tel.: +1-573-341-4945; fax: +1-573-341-4115.

E-mail address: tsai@umr.edu (H.L. Tsai).

0017-9310/01/$ - see front matter
PII: S0017-9310(00)00094-6

Nomenclature

a_i	activity of species i in solution
A_γ	negative of $d\gamma/dT$ for a pure Fe system
B_θ	azimuthal magnetic field
c_p	specific heat
f_L	liquid fraction
g	gravitational acceleration
h_c	combined heat transfer coefficient
j_n	current density distribution normal to top surface
j_r, j_z	radial, axial current density
k	thermal conductivity
k_1	constant related to entropy of segregation
K	defined in Eq. (10)
M, N	total number of nodes in ξ- and ζ-directions
n	normal direction to surface
P	pressure
P_{arc}	arc pressure acting on top surface
q_n	heat flux distribution normal to top surface
r, z	radial, axial coordinate
r_T	radius of molten pool at top surface
r_B	radius of molten pool at bottom surface
R_g	gas constant
s	tangential direction along a surface
S	source term
t	time
T	temperature
T_∞	surrounding temperature
T_L	liquidus temperature
T_S	solidus temperature
u, w	radial, axial velocity
V_n	normal velocity component at molten pool surface
V_s	tangential velocity component at molten pool surface
ΔH	latent heat of fusion
ΔH_0	standard heat of adsorption

Greek symbols

γ	surface tension
γ_m	surface tension at melting temperature
$d\gamma/dT$	temperature gradient of surface tension
Γ_s	surface excess at saturation
ε	radiation emissivity
ε_Φ	error of convergence
λ	Largrange multiplier
μ	viscosity
μ_0	magnetic permeability
ξ, ζ	transformed coordinate system
ρ	density
σ	electrical conductivity
τ_a	arc drag force acting on top surface
ϕ	electrical potential
φ	displacement of the top surface
ψ	displacement of the bottom surface
Φ	general dependent variable

tungsten arc (GTA) weld pool with full penetration. This situation is due to the complexity of the coupling of the free surface on the bottom of the pool, the deformation of the top pool surface, and the temperature distribution. In a study by Nishiguchi et al. [11], a purely heat conductive, rather than convective, model was used in arc welding of a thin plate with full penetration. Na and Lho [12] also used a purely heat conductive model to describe the weld pool surface profile in circumferential gas tungsten arc welding (GTA) of small pipes. Recently, a three-dimensional steady model describing heat and fluid flow in fully penetrated GTA weld pool was presented by Zhang et al. [13]. In their study, however, the influence of arc drag force and the latent heat effect were not included, and the temperature coefficient of surface tension on the pool surface was assumed to be a negative constant.

The objective of this work is to develop a numerical model for partially or fully penetrated weld pools in stationary GTAW. Considering the above-mentioned four driving forces, heat transfer and fluid flow of weld pool have been calculated at different welding times until full penetration occurs. In the numerical simulation, difficulties associated with the irregular weld pool surface profile and the moving liquid–solid interface have been overcome by adopting a boundary fitted coordinate. Special attention has been given to the deformation of the top and the bottom weld pool surfaces under arc pressure. The calculated GTA weld bead geometry shows favorable agreement with experimental results.

2. Mathematical formulation

Fig. 1 shows a schematic diagram of the coordinate system and the driving forces acting on the molten pool. Flow in the pool is driven by a combination of buoyancy, electromagnetic, surface tension, and arc drag force. In order to simplify the mathematical model, the following assumptions have been made: (1) the welding process is restricted to the stationary GTA

spot welding, and the system is axisymmetric; (2) laminar flow is assumed since the size of the pool is small; (3) the thermophysical properties are assumed constant, except the temperature-dependent surface tension; and (4) the transport phenomena into the workpiece are determined from the numerical analysis of the welding arc under the assumption of a rigid surface at anode [14,15]. In other words, surface deformation of the weld pool does not affect the calculated transport phenomena (heat flux, current density, arc drag force, and arc pressure; see Fig. 3) from the welding arc.

Based on the above assumptions, the governing differential equations in the r–z coordinate system can be expressed as follows:

Continuity

$$\frac{1}{r}\frac{\partial(\rho r u)}{\partial r}+\frac{\partial(\rho w)}{\partial z}=0 \tag{1}$$

Momentum

$$\frac{\partial(\rho u)}{\partial t}+\frac{1}{r}\frac{\partial}{\partial r}\left(\rho r u u-\mu r\frac{\partial u}{\partial r}\right)+\frac{\partial}{\partial z}\left(\rho u w-\mu\frac{\partial u}{\partial z}\right)=-\frac{\partial P}{\partial r}+\frac{1}{r}\frac{\partial}{\partial r}\left(\mu r\frac{\partial u}{\partial r}\right)-2\mu\frac{u}{r^2}+\frac{\partial}{\partial z}\left(\mu\frac{\partial w}{\partial r}\right)-j_z B_\theta \tag{2}$$

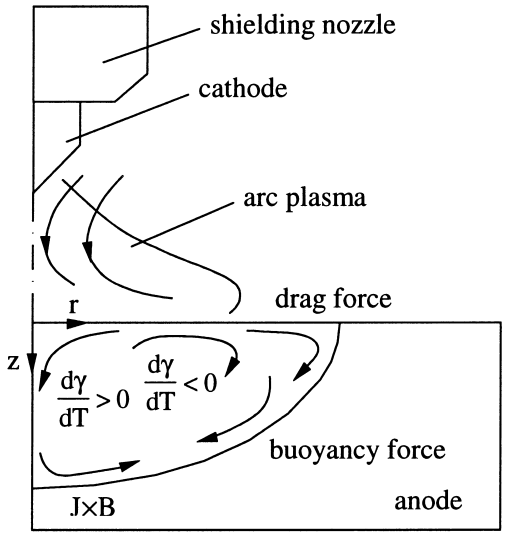

Fig. 1. Schematic diagram of the coordinate system and driving forces acting on a GTAW molten pool.

$$\frac{\partial(\rho w)}{\partial t}+\frac{1}{r}\frac{\partial}{\partial r}\left(\rho r u w-\mu r\frac{\partial w}{\partial r}\right)+\frac{\partial}{\partial z}\left(\rho w w-\mu\frac{\partial w}{\partial z}\right)=-\frac{\partial P}{\partial z}+\frac{1}{r}\frac{\partial}{\partial r}\left(\mu r\frac{\partial u}{\partial z}\right)+\frac{\partial}{\partial z}\left(\mu\frac{\partial w}{\partial z}\right)+\rho g\beta(T-T_{\mathrm{L}})+j_r B_\theta \tag{3}$$

Energy

$$\frac{\partial(\rho c_p T)}{\partial t}+\frac{1}{r}\frac{\partial}{\partial r}\left(r\rho c_p u T-rk\frac{\partial T}{\partial r}\right)+\frac{\partial}{\partial z}\left(\rho c_p w T-k\frac{\partial T}{\partial z}\right)=-\rho\Delta H\frac{\partial f_{\mathrm{L}}}{\partial t} \tag{4}$$

In the energy equation, latent heat of fusion is included by employing the liquid fraction, f_{L}, which is defined as follows:

$$f_{\mathrm{L}}=1 \quad \text{for } T>T_{\mathrm{L}}$$

$$f_{\mathrm{L}}=\frac{T-T_{\mathrm{S}}}{T_{\mathrm{L}}-T_{\mathrm{S}}} \quad \text{for } T_{\mathrm{S}}\le T\le T_{\mathrm{L}}$$

$$f_{\mathrm{L}}=0 \quad \text{for } T<T_{\mathrm{S}} \tag{5}$$

where T_{L} and T_{S} are the liquidus and solidus temperature, respectively.

2.1. Electrical charge

In order to obtain the electromagnetic force terms in Eqs. (2) and (3), electric potential ϕ is calculated by solving the equation for current continuity,

$$\frac{1}{r}\frac{\partial}{\partial r}\left(\sigma r\frac{\partial\phi}{\partial r}\right)+\frac{\partial}{\partial z}\left(\sigma\frac{\partial\phi}{\partial z}\right)=0 \tag{6}$$

and current density is calculated from Ohm's law,

$$j_r=-\sigma\frac{\partial\phi}{\partial r};\qquad j_z=-\sigma\frac{\partial\phi}{\partial z} \tag{7}$$

while the self-induced azimuthal magnetic field is derived from Ampere's law.

$$B_\theta=\frac{\mu_0}{r}\int_0^r j_z r\,\mathrm{d}r. \tag{8}$$

2.2. Surface tension

Many researchers have reported the importance of surface tension and the relationship between the temperature gradients of surface tension and the amount of minor elements such as S, O, and Se. However, experimental surface tension data are seldom available

for any material throughout the temperature range of interest. In the present study, the temperature-dependent surface tension for Fe–S alloys as a function of both temperature and composition is obtained from a recently developed formalism [2].

$$\gamma = \gamma_m - A_\gamma(T - T_L) - R_g T \Gamma_S \ln(1 + Ka_i) \tag{9}$$

$$\text{where } K = k_1 \exp\left(-\frac{\Delta H_0}{R_g T}\right) \tag{10}$$

2.3. Boundary conditions

The solution domains used in this study are shown in Fig. 2 for partially and fully penetrated weld pools. Two different domains are used, one is ACDE for solving the electrical potential and temperature field, and the other is ABF for the momentum equations, because the fluid flow takes place only within the fusion region. The ACDE domain contains 40 nodes in the r-direction and 35 nodes in the z-direction. The number of nodes in the ABF domain is adjusted in the progress of calculations according to the molten pool size. The boundary fitted nodes are used for describing the fusion boundary.

The boundary conditions for solving the governing equations are as follows:

(1) *At the top surface AFE*

$$j_n(r) = -\sigma\frac{\partial \phi}{\partial n} \tag{11}$$

$$q_n(r) = -k\frac{\partial T}{\partial n} \tag{12}$$

In addition, when a molten pool forms, the following condition must be satisfied along its surface (i.e., AF)

$$-\mu\frac{\partial V_s}{\partial n} = \tau_a + \frac{d\gamma}{dT}\frac{\partial T}{\partial s}, \qquad V_n = 0 \tag{13}$$

where $j_n(r)$, $q_n(r)$, and τ_a are the distribution of current density, heat flux, and arc drag force acting on the surface of molten pool. Instead of assuming a Gaussian distribution [1–4], the calculated heat flux,

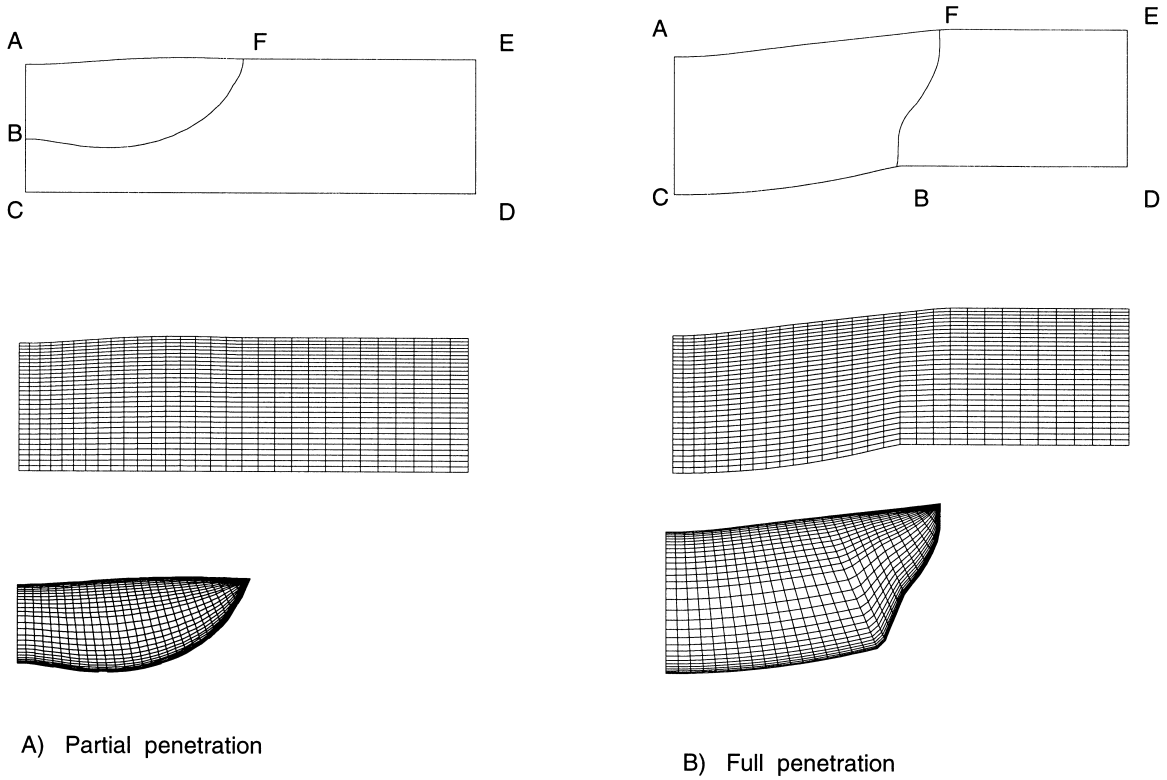

Fig. 2. Solution domain for analyzing molten pool and mesh generation with boundary-fitted coordinates.

current density, and arc drag force from Ref. [15] for a 150 A, 3 mm long welding arc, as shown in Fig. 3, are used in the present study (the aforementioned fourth assumption). The algorithm used in modeling heat and fluid flow in a welding arc is detailed in Ref. [15].

(2) *At the axisymmetrical axis AC*

$$u = 0, \qquad \frac{\partial w}{\partial r} = 0 \tag{14}$$

$$\frac{\partial \phi}{\partial r} = 0 \tag{15}$$

$$\frac{\partial T}{\partial r} = 0 \tag{16}$$

(3) *At the outer surface DE*

$$\frac{\partial \phi}{\partial r} = 0 \tag{17}$$

$$-k\frac{\partial T}{\partial r} = h_c(T - T_\infty) \tag{18}$$

where h_c is the combined heat transfer coefficient for the radiative and convective boundary expressed in the

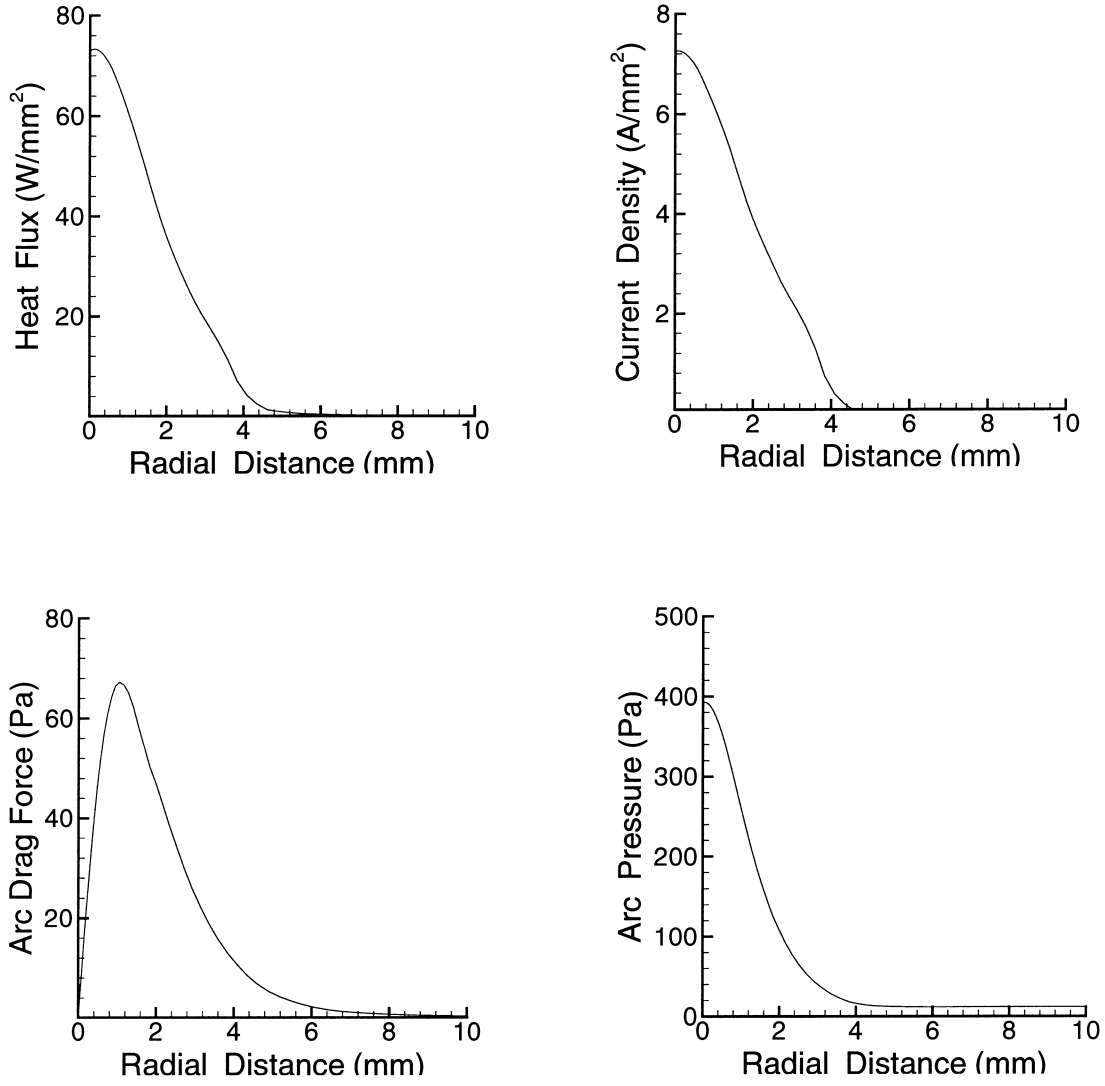

Fig. 3. Calculated transporting phenomena to weld pool from Ref. [15] (current: 150 A, arc length 3 mm).

following equation [16]

$$h_c = 24.1 \times 10^{-4} \varepsilon T^{1.61} \tag{19}$$

(4) *At the bottom surface CD*

$$\phi = \phi|_{\text{const}} \tag{20}$$

$$-k\frac{\partial T}{\partial n} = h_c(T - T_\infty) \tag{21}$$

If full penetration occurs, the following additional conditions must be satisfied along CB

$$\mu\frac{\partial V_s}{\partial n} = \frac{d\gamma}{dT}\frac{\partial T}{\partial s}, \qquad V_n = 0 \tag{22}$$

(5) *Along the solid–liquid interface BF*

$$u = 0, \qquad w = 0 \tag{23}$$

2.4. Surface deformation

The surface depression will form a shape which minimizes the total energy. The weld pool is distorted by the gravitational force, arc pressure, and surface tension acting on the weld pool. The equations governing the top and the bottom surface profile of the weld pool take the following forms [11–13]

$$\gamma\left\{\frac{r\varphi_{rr} + \varphi_r(1+\varphi_r^2)}{r(1+\varphi_r^2)^{3/2}}\right\} = \rho g\varphi - P_{\text{arc}} + \lambda \tag{24}$$

$$-\gamma\left\{\frac{r\psi_{rr} + \psi_r(1+\psi_r^2)}{r(1+\psi_r^2)^{3/2}}\right\} = \rho g(\psi + L - \varphi) + \lambda \tag{25}$$

where φ and ψ represent, respectively, the displacement of the top and the bottom surface of the weld pool. The arc pressure distribution given in Fig. 3 (obtained from Ref. [15]) is used and $\varphi_r = \dfrac{\partial\varphi}{\partial r}$, $\varphi_{rr} = \dfrac{\partial^2\varphi}{\partial^2 r}$, etc.

The boundary conditions for solving Eqs. (24) and (25) are:

At the center

$$\frac{\partial\varphi}{\partial r} = 0, \qquad \frac{\partial\psi}{\partial r} = 0 \tag{26}$$

At the end of the melting zone (i.e., point F for partial penetration, and points F and B for full penetration)

$$\varphi = 0, \qquad \psi = 0. \tag{27}$$

Since the total volume of the molten pool is assumed to be the same as the original base metal, the constant λ can be determined from the following constraint condition:
For partial penetration

$$\int_0^{r_T} 2\pi\varphi r\, dr = 0 \tag{28}$$

For full penetration

$$\int_0^{r_T} 2\pi\varphi r\, dr = \int_0^{r_B} 2\pi\psi r\, dr \tag{29}$$

3. Numerical procedure

3.1. Domain transformation

The physical domain represented by a boundary-fitted coordinate system must be transformed into a rectangular domain (computational domain) before a standard finite difference method can be applied to the solution of the governing differential equations discussed above. By using a general dependent variable, Φ, the governing equations can be expressed in the following generalized form:

$$\frac{\partial(\rho\Phi)}{\partial t} + \frac{1}{r}\frac{\partial}{\partial r}\left(\rho ru\Phi - r\Gamma_\Phi\frac{\partial\Phi}{\partial r}\right) + \frac{\partial}{\partial z}\left(\rho w\Phi - \Gamma_\Phi\frac{\partial\Phi}{\partial z}\right) = S_\Phi \tag{30}$$

where Γ_Φ is the general diffusion coefficient and S_Φ, representing all other terms not included in the first three terms, is regarded as the source term. Eq. (30) was then transformed to a generalized curvilinear coordinate system as shown in Fig. 4, resulting in the following equation [15]:

$$\begin{aligned}\frac{\partial(\rho\Phi)}{\partial t} &+ \frac{1}{r}\frac{\partial}{\partial\xi}\left\{\rho ru\Phi - r\Gamma_\Phi\left(\frac{\partial\Phi}{\partial\xi}\frac{\partial\xi}{\partial r} + \frac{\partial\Phi}{\partial\zeta}\frac{\partial\zeta}{\partial r}\right)\right\}\frac{\partial\xi}{\partial r} \\ &+ \frac{1}{r}\frac{\partial}{\partial\zeta}\left\{\rho ru\Phi - r\Gamma_\Phi\left(\frac{\partial\Phi}{\partial\xi}\frac{\partial\xi}{\partial r} + \frac{\partial\Phi}{\partial\zeta}\frac{\partial\zeta}{\partial r}\right)\right\}\frac{\partial\zeta}{\partial r} \\ &+ \frac{\partial}{\partial\xi}\left\{\rho w\Phi - \Gamma_\Phi\left(\frac{\partial\Phi}{\partial\xi}\frac{\partial\xi}{\partial z} + \frac{\partial\Phi}{\partial\zeta}\frac{\partial\zeta}{\partial z}\right)\right\}\frac{\partial\xi}{\partial z} \\ &+ \frac{\partial}{\partial\zeta}\left\{\rho w\Phi - \Gamma_\Phi\left(\frac{\partial\Phi}{\partial\xi}\frac{\partial\xi}{\partial z} + \frac{\partial\Phi}{\partial\zeta}\frac{\partial\zeta}{\partial z}\right)\right\}\frac{\partial\zeta}{\partial z} = S_\Phi\end{aligned} \tag{31}$$

where

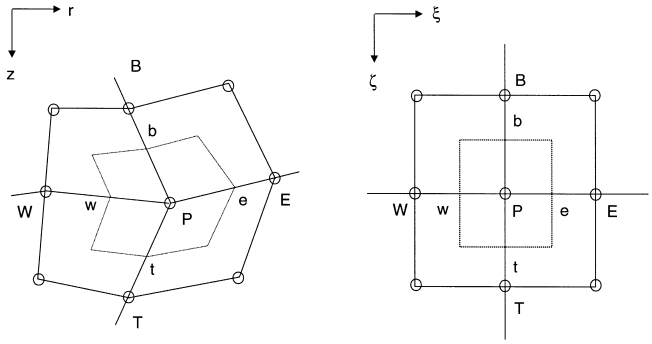

Fig. 4. Geometric transformation and grid-structure with notation.

$$\frac{\partial \xi}{\partial r} = \frac{1}{J}\frac{\partial z}{\partial \zeta}, \quad \frac{\partial \zeta}{\partial r} = -\frac{1}{J}\frac{\partial z}{\partial \xi}, \quad \frac{\partial \xi}{\partial z} = -\frac{1}{J}\frac{\partial r}{\partial \zeta}, \quad \frac{\partial \zeta}{\partial z} = \frac{1}{J}\frac{\partial r}{\partial \xi}, \quad J = \frac{\partial r}{\partial \xi}\frac{\partial z}{\partial \zeta} - \frac{\partial r}{\partial \zeta}\frac{\partial z}{\partial \xi}. \tag{32}$$

The transformation coefficients were calculated numerically using the second-order central difference method. In the transformed domain, the grid size was set to be unity for simplifying the calculation.

3.2. Numerical method

The transformed equation (31) is discretized using the control volume approach in the transformed domain as shown in Fig. 4, which results in an equation in the following form:

$$a_P \Phi_P = a_E \phi_E + a_W \Phi_W + a_T \Phi_T + a_B \Phi_B + S \tag{33}$$

where the general dependent variable Φ can be any of u, w, T, P or ϕ. The values of a_P, a_E, etc. are the coefficients resulting from Eqs. (1)–(7), and S is the source term from Eqs. (1)–(7). Variables of the equations are solved iteratively, and the numerical iteration procedure is summarized in Fig. 5.

Convergence is declared when the following condition is satisfied.

$$\frac{\sum_{i=1}^{M}\sum_{k=1}^{N}\left|\Phi_{i,k}^{m} - \Phi_{i,k}^{m-1}\right|}{\Phi_{\max}} < \varepsilon_\Phi, \quad \varepsilon_\Phi = 0.01 \tag{34}$$

where M and N are the total number of nodes in the r and z directions, respectively, and m is the number of iterations. The dimension of the computational domain is 10 mm in the r direction and 5 mm in the z direction. A fixed, non-uniform grid system (Fig. 2) was used in the present study. Accuracy of the computed results was assured by refining the grid system until no additional change of the results was obtained.

4. Experimental procedure

A DC (direct current), constant current power source is used to make the stationary spot welds, while the welding time is regulated by a timer installed in the welding equipment. The electrode of 3.2 mm diameter, 60° tip angle and 2% thoriated tungsten is used throughout the experiments. The material is a type 304 stainless steel of 3 mm thickness and its composition is shown in Table 1. This plate is cut to size 50 mm × 50 mm and ground smooth. Each specimen is also cleaned

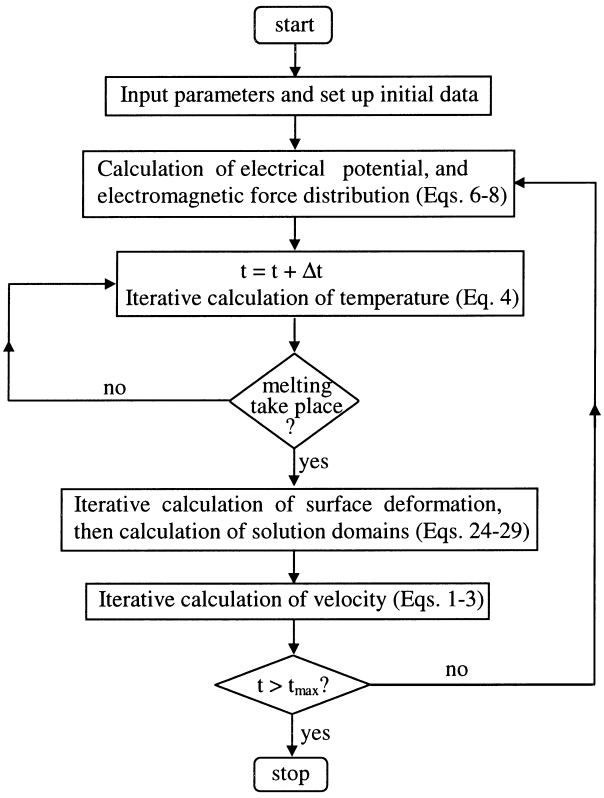

Fig. 5. Flow diagram of calculations.

Table 1
Welding conditions and material properties for AISI-304 stainless steel

Nomenclature	Symbol	Value
Activity of sulfur	a_i	0.022 wt%
Coefficient of thermal expansion	β	10^{-4} K^{-1}
Constant in surface tension coefficient	A_γ	4.3×10^{-4} N/m K
Density	ρ	7200 kg/m^3
Electrical conductivity	σ	7.7×10^5 Ω^{-1} m^{-1}
Radiation emissivity	ε	0.9
Gas constant	R_g	8314.3 J/kg mole K
Latent heat of fusion	ΔH	2.47×10^5 J/kg
Liquidus temperature	T_L	1723 K
Magnetic permeability	μ_0	1.26×10^{-6} H/m
Solidus temperature	T_S	1523 K
Surrounding temperature	T_∞	293 K
Specific heat	c_p	753 J/kg K
Standard heat of adsorption	ΔH_0	-1.66×10^8 J/kg mole
Surface excess at saturation	Γ_S	1.3×10^{-8} kg mole/m^2
Entropy factor	k_1	0.00318
Surface tension at pure metal	γ_m	1.943 N/m
Thermal conductivity	k	20 W/m K
Viscosity	μ	0.05 kg/m s

with acetone before welding. The welding is conducted under the condition of 150 A welding current and 3 mm arc length [15]. The specimens are quenched at several predetermined instants, and then are cut, polished and etched so that the weld pool shape can be clearly seen.

5. Results and discussion

It is a well-established fact that the fluid flow and heat transfer in the weld pool are dominated by the spatial variation of surface tension, which, in turn, is due to the temperature gradient of surface tension, $d\gamma/dT$. The calculated $d\gamma/dT$ for type 304 stainless steels (220 ppm sulfur) as a function of temperature is given in Fig. 6. It is seen that $d\gamma/dT$ is positive until the temperature reaches approximately 2400 K; it then becomes negative for higher temperatures.

Fig. 7 shows the calculated flow patterns inside the molten pool at different times during welding. The velocity distributions are plotted on the right-hand side, while the streamlines are plotted on the left. In order to better show the direction of the fluid flow, uniform-length velocity vectors are used on the right-hand side for $t = 3$ and 4 s. When the weld pool is partially penetrated, the fluid flow at the weld pool surface is radically outward, creating a single clockwise vortex in the molten pool. This is caused by the negative temperature surface tension gradient, $d\gamma/dT$, and by the arc drag force on the top pool surface. As the arc heat flux is at its highest in the center of the weld pool (Fig. 3), the surface temperature of the weld pool decreases outward. As the surface temperature of the weld pool is above 2400 K, according to Fig. 6, a greater surface tension occurs near the edge of the weld pool, pulling the fluid at the weld pool surface outward.

After achieving full penetration, a bifurcated flow gradually appears in the weld pool. As shown in the left-hand plot of Fig. 7, there is a large counterclockwise vortex near the upper portion of the weld pool at $t = 3$ s, while near the center and in the lower portion of the weld pool, another small counterclockwise vor-

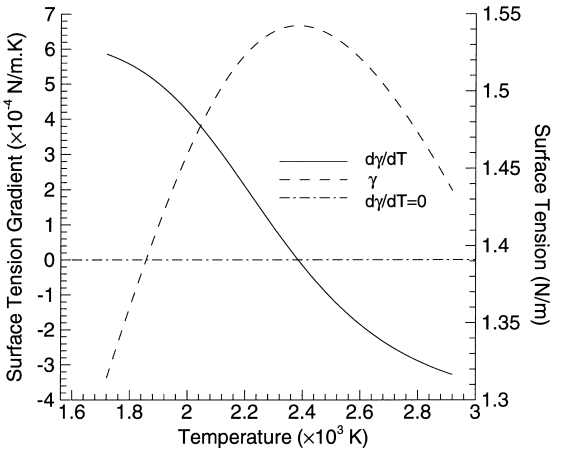

Fig. 6. Surface tension and its gradients as a function of temperature for 220 ppm sulfur.

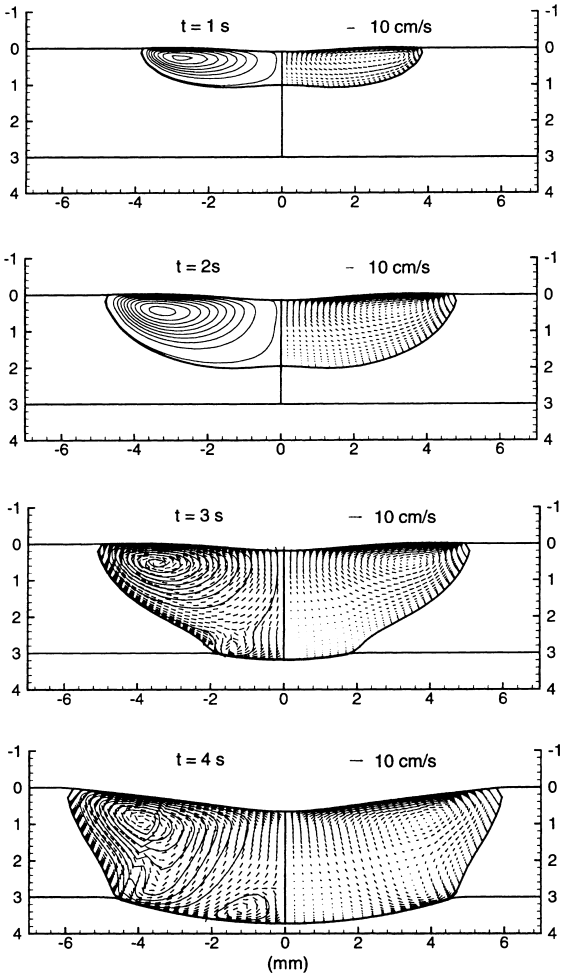

Fig. 7. Computed flow pattern in the molten pool.

tex is developing. However, at $t = 4$ s the large counterclockwise vortex remains similar to that at $t = 3$ s, but the small counterclockwise vortex has changed to a clockwise vortex. If one uses the maximum flow velocity (about 7 cm/s) and diameter of the weld pool (about 10 mm) as, respectively, the characteristic velocity and characteristic length, the Reynolds number is found to be about 100. Hence, the assumption of laminar flow in the weld pool appears to be appropriate in the present study.

In order to understand the transition of the flow pattern near the lower portion of the weld pool when the weld pool is fully penetrated, a temperature distribution along the bottom pool surface is plotted in Fig. 8. As shown in the figure, since the temperature on the bottom pool surface is under the critical temperature 2400 K, $d\gamma/dT$ is positive everywhere on the bottom pool surface. At $t = 3$ s, the maximum surface tension occurs at the center of the weld pool pulling

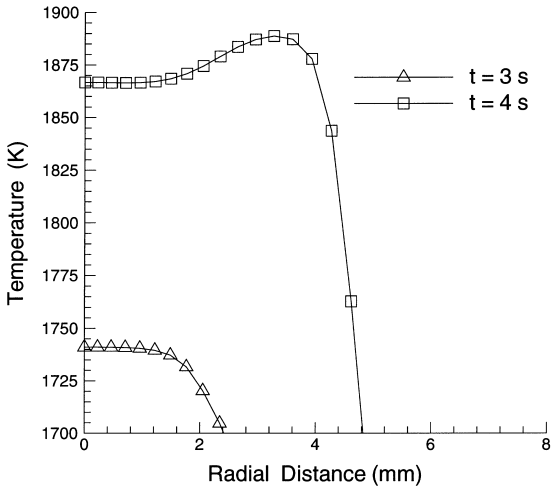

Fig. 8. Radial temperature distribution on the bottom pool surface.

the bottom surface fluid to the center and creating a counterclockwise vortex. However, at $t = 4$ s, the bottom surface temperature, as shown in Fig. 8, achieves its highest in the middle but slightly toward the edge of the weld pool. Therefore, the surface tension in the middle of the bottom pool surface is the highest, pulling the surface fluid from both sides and creating a clockwise vortex near the center of the weld pool. It is interesting to see that the change of temperature distribution along the bottom free surface is caused by the large upper vortex which brings heat from the top free surface downward.

The importance of surface tension and arc drag force in determining fluid flow in the weld pool can be further understood by using Eq. (13), Figs. 3 and 6, and temperature distribution along the free surface (e.g., Fig. 8). From Fig. 3, it is seen that arc drag force is zero at the arc center, which abruptly reaches its maximum (about 68 N/m^2) at a radial distance about 1.2 mm from the center, and then rapidly decreases to zero. It is noted that the arc drag force is always acting in the direction outward; while the surface tension temperature gradient ($d\gamma/dT$) decreases as temperature increases, reaches zero at $T = 2400$ K, and becomes negative thereafter, Fig. 6. As the top surface temperature of the weld pool is above 2400 K and decreases outward, the spacial temperature gradient ($\partial T/\partial s$, Eq. (13)) is negative. As a result, the surface tension force is outward (positive) as is the drag force, leading to an outward surface flow. As discussed in Ref. [17], the magnitude of arc drag force is equal to or slightly greater than the surface tension force in arc welding. However, there is no arc drag force at the bottom free surface, and the free surface temperatures are lower (Fig. 8), as compared to those in the top free surface, resulting in all positive values of $d\gamma/dT$. In Fig. 8, at $t = 3$ s, $\partial T/\partial s$ is negative, leading to a negative surface tension force and an inward flow at the bottom free surface. However, at $t = 4$ s, the sign of $\partial T/\partial s$ changes from positive to negative along the radial direction, resulting in an outward surface flow near the center at the weld pool bottom, as discussed before. From the

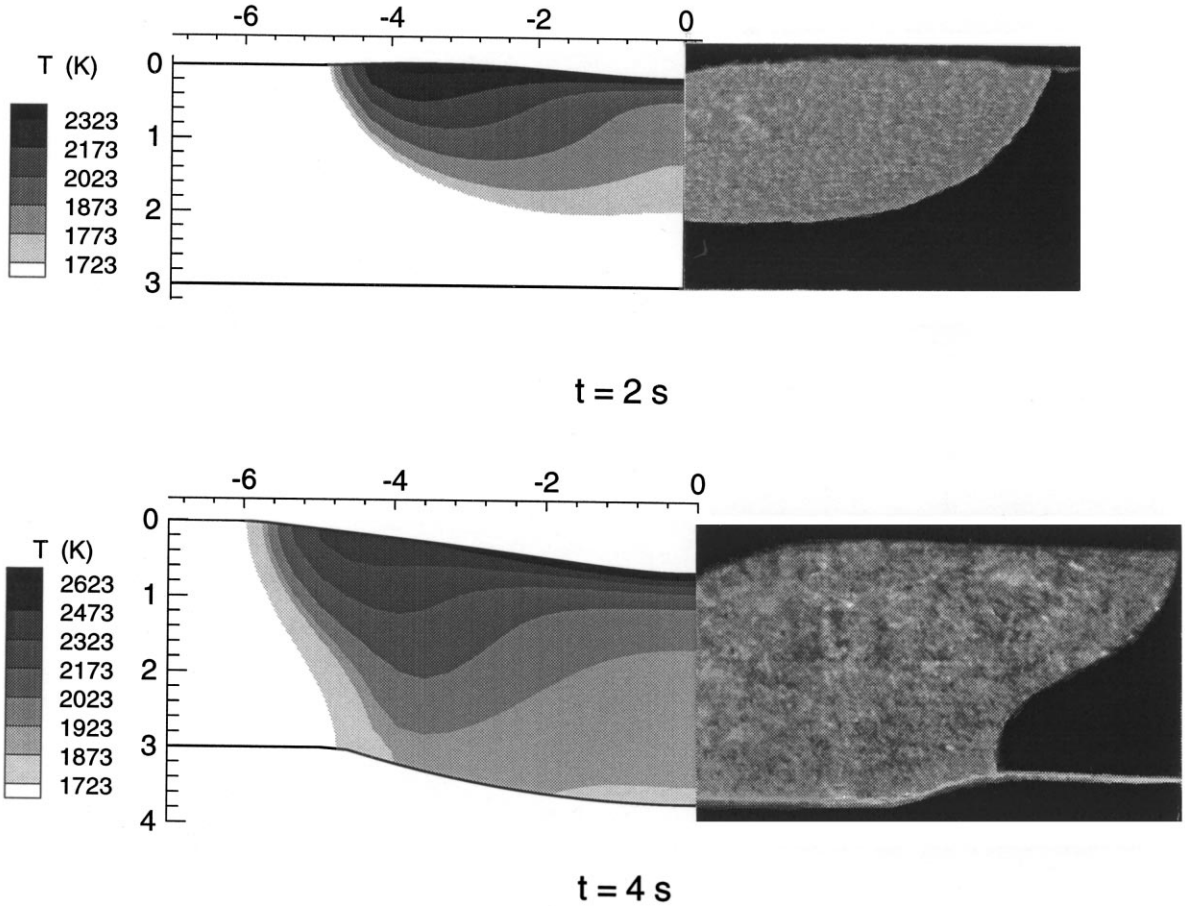

Fig. 9. Comparison of the calculated and experimentally observed weld fusion zone.

aforementioned discussion, it can be concluded that surface tension plays a critical role in determining the flow pattern in the weld pool.

The experimentally observed and the predicted results of GTA welding with 150 A current and 3 mm arc length are presented in Fig. 9. It is noted that the liquidus temperature of 304 stainless steel used in the present study is 1723 K. Hence, at $t = 2$ s or 4 s, the shaded area in the left-hand side of Fig. 9 represents the weld pool shape. The "spoon" shape of the temperature contours shows the significant influence that fluid flow has on the temperature distribution in the weld pool. As seen in Fig. 9, especially at $t = 4$ s, the experimental results show some depression of the weld bead top surface near the center, slightly convex in the middle, and then a little downward near the edge of the weld bead. Although the predicted weld pools have a depression in the center, the model fails to predict a convex shape in the middle of the weld pool and the depression near the edge of the weld bead. As indicated by the figure, the weld bead surface depression is not significant for a partial penetration weld pool. In a fully penetrated weld, however, the top surface depression is large, which is caused by the "sagged" free bottom surface. By considering the complexity of a GTAW process, assumptions used in the model, and imperfect matching of welding conditions used in experiments and modeling, the agreement between the predicted and the experimentally observed fusion zone shape and size is felt to be reasonably good.

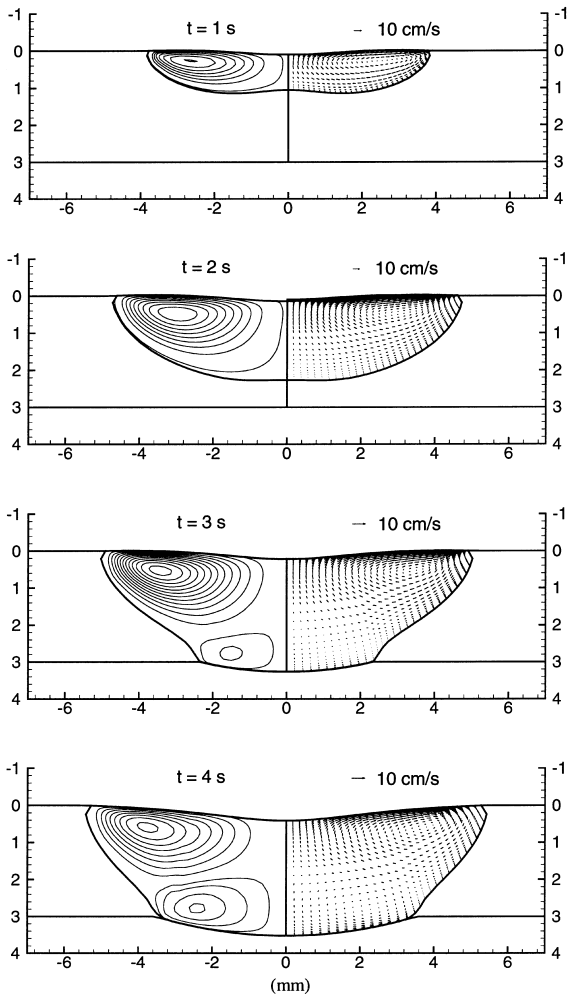

Fig. 10. Computed flow pattern in the molten pool ($d\gamma/dT = -0.112 \times 10^{-3}$ N/m K).

In the study by Zhang et al. [13], a constant temperature coefficient of surface tension ($d\gamma/dT = -0.112 \times 10^{-3}$ N/m K) was assumed. As indicated in their study, the flow patterns were similar in partially and fully penetrated weld pools for a three-dimensional moving arc weld. For purposes of comparison, in this study, a constant $d\gamma/dT = -0.112 \times 10^{-3}$ N/m K is also assumed in stationary spot welding. As seen in Fig. 10, the flow patterns are different in partially and fully penetrated weld pools for stationary spot welding. Owing to the assumption of negative $d\gamma/dT$, the highest surface tension is reached at the edge of the weld pool, while the surface tension at the arc center is the lowest. In the case of full penetration, the molten metal flows outward from the arc center in both the top and the bottom pool surface, so that a bifurcated flow pattern is obtained in the weld pool. However, it is clearly seen that the flow pattern at $t = 4$ s in Fig. 10 is different from the corresponding pattern in Fig. 7.

6. Conclusions

A two-dimensional heat and fluid flow model has been developed to analyze a partially or fully penetrated weld pool in stationary GTA welding. In addition to temperature distribution and velocity field, deformations of the top and the bottom pool free surfaces were calculated.

For a fully penetrated weld pool, the additional free surface appearing on the bottom of the workpiece tends to increase the depression of the top weld pool surface. Surface tension was found to play an important role in determining the flow pattern in the weld pool. Especially, for a full penetration weld, surface tension on the bottom pool surface can significantly affect the flow field in the weld pool. Under the welding conditions used in the present study, a bifurcated flow pattern was predicted due to the positive gradient of surface temperature, $d\gamma/dT$, and the distribution of temperature along the bottom free surface. The calcu-

lated weld bead shape compares favorably with the experimental results.

Acknowledgements

This work was supported by the U.S. Army Research Office under grant number DAAH-95-1-0136 which is gratefully acknowledged.

References

[1] Y.P. Lei, Y.W. Shi, Numerical treatment of the boundary conditions and source terms on a spot welding process with combining buoyancy-Marangoni-driven flow, Numerical Heat Transfer 26B (1994) 455–471.
[2] A. Matunawa, S. Yokoya, Y. Asako, Convection in weld pool and its effect on penetration shape in stationary arc welds, Q. J. of Japan Welding Society 6 (1987) 3–10.
[3] T. Zacharia, S.A. David, J.M. Vitek, T. DebRoy, Weld pool development during GTA and laser beam welding of Type 304 stainless steel, part 1 — theoretical analysis, Welding Journal 68 (1989) 499s–509s.
[4] K.C. Tsao, C.S. Wu, Fluid flow and heat transfer in GMA weld pools, Welding Journal 67 (1988) 70s–75s.
[5] R.T.C. Choo, J. Szekely, S.A. David, On the calculation of the free surface temperature of gas–tungsten arc weld pools from first principles: part 2. Modeling the weld pool and comparison with experiments, Metall. Trans. B 23B (1992) 371–384.
[6] T. Zacharia, A.H. Eraslan, K.K. Aidun, Modeling of autogenous welding, Welding Journal 67 (1988) 53s–62s.
[7] T. Zacharia, A.H. Eraslan, K.K. Aidun, Modeling of nonautogenous welding, Welding Journal 67 (1988) 18s–27s.
[8] R.T.C. Choo, J. Szekely, R.C. Westhoff, Modeling of high current arcs with emphasis on free surface phenomena in the weld pool, Welding Journal 69 (1990) 346s–361s.
[9] M.C. Tsai, S. Kou, Electromagnetic-force-induced convection in weld pools with a free surface, Welding Journal 69 (1990) 241s–246s.
[10] S.D. Kim, S.J. Na, Effect of weld pool deformation on weld penetration in stationary gas tungsten arc welding, Welding Journal 71 (1992) 179s–193s.
[11] K. Nishiguchi, T. Ohji, N. Nakata, K. Ishibashi, Study on behavior of molten pool in arc welding (mathematical modeling of a molten pool in arc welding of thin plate), Q. J. of Japan Welding Society 2 (1984) 201–207.
[12] S.J. Na, T.J. Lho, A study on parameter optimization for circumferential gas tungsten arc (GTA) welding of small pipes considering backing gas pressure, part 1: analysis of weld pool surface profile, Proc. Instn. Mech. Engr. Part B: Journal of Engineering Manufacture 210 (1996) 77–85.
[13] Y.M. Zhang, Z.N. Cao, R. Kovacevic, Numerical analysis of fully penetrated weld pools in gas tungsten arc welding, Proc. Instn. Mech. Engr. Part C: Journal of Mechanical Engineering Science 210 (1996) 187–195.
[14] H.G. Fan, Y.W. Shi, Numerical simulation on arc pressure of gas tungsten arc welding, J. of Mater. Process Technol 61 (1996) 302–308.
[15] S.Y. Lee, S.J. Na, Analysis of TIG welding arc using boundary-fitted coordinate, Proc. Instn. Mech. Engr. Part B: Journal of Engineering Manufacture 209 (1995) 153–164.
[16] J. Goldak, M. Bibby, J. Moore, B. Patel, Computer modeling of heat flow in welds, Metall. Trans. 17B (1986) 587–600.
[17] W.H. Kim, H.G. Fan, S.J. Na, Effect of various driving forces on heat and mass transfer in arc welding, Numerical Heat Transfer, Part A 32 (1997) 633–652.